Supporting Information

Material and Methods

Protein preparation and labeling. Cysteine residues for the specific labeling of IDPs using maleimide chemistry were introduced by site-directed mutagenesis at the positions given in Table S1. ProTα (57) variants, IN (58) and ACTR (59) were produced in E. coli BL21 with an N-terminal His-tag for purification. Cells were grown in LB medium and expression was induced with IPTG.

Disruption of harvested cells and ammonium sulfate precipitation were carried out as described previously for ProTα (60). The protein was bound to a gravity flow Ni-NTA column (Thermo Scientific) and eluted with 20 mM Tris, 100 mM sodium chloride, and 500 mM imidazole, pH 7.5. The sample was dialyzed against 20 mM Tris, 100 mM sodium chloride, and 20 mM imidazole, pH 7.5. The His-tag was cleaved off with HRV 3C protease, which also contained a His-tag; a second Ni-NTA chromatography run was used to remove the protease and the His-tag. The flow-through containing ProTα was concentrated with a YM-3 Centriprep centrifugal filter (Merck Millipore), reduced with 10 mM TCEP, and purified by reversed phase (RP) HPLC on a Reprosil Gold 200 column (Dr. Maisch, Germany) and elution with an acetonitrile gradient. Purified ProTα was lyophilized in a SpeedVac concentrator (Thermo Scientific), dissolved in 0.1 M sodium phosphate, pH 7.5, and labeled with Alexa Fluor 488 maleimide (Invitrogen) at a molar ratio of dye to protein of 0.8:1. The reaction mixture was quenched with β-mercaptoethanol, reduced with 10 mM TCEP and purified by RP-HPLC on an XTerra C18 column (Waters). The fraction containing singly labeled ProTα was lyophilized in a SpeedVac concentrator, and labeled and purified analogously with a molar excess of Alexa Fluor 594 maleimide (Invitrogen). The masses of the doubly labeled ProTα-N and ProTα-C were confirmed by electrospray ionization mass spectrometry (ESI-MS).

IN was purified by Ni-NTA chromatography as described for ProTα. The His-tag was removed by enzymatic cleavage with Thrombin protease after dialysis against 50 mM NaHCO$_3$ pH 9.3, 0.5 M Na$_2$SO$_4$, 0.1 M NaCl, 5 mM EDTA, 1 mM DTT. After reduction with 10 mM TCEP and purification by RP-HPLC, IN was lyophilized in a SpeedVac concentrator, dissolved in 50 mM HEPES, 0.5 mM ZnCl$_2$, and 0.5 M arginine, pH 7.5, and labeled with Alexa Fluor 488 maleimide at a molar ratio of dye to protein of 0.8:1. The reaction mixture was quenched with β-mercaptoethanol, reduced with 10 mM TCEP and purified by RP-HPLC on a XTerra C18 column. The fraction containing singly labeled IN was lyophilized in a SpeedVac concentrator, and labeled and purified analogously with Alexa Fluor 594 maleimide. The doubly labeled IN was purified by RP-HPLC on an XTerra C18 column. The correct mass of the labeled IN was confirmed by ESI-MS.

ACTR was co-expressed with NCBD (nuclear co-activator binding domain of CREB) to improve the stability of ACTR during expression (59). The harvested cells were disrupted with a TS 1.1 cell disruption system (Constant Systems Ltd, England), the protein was bound to a Ni-NTA column, and the His-tag was removed by enzymatic cleavage with HRV 3C protease. After reduction of the sample with β-mercaptoethanol, the protease and the His-tag were removed with a second Ni-NTA column. ACTR was separated from NCBD by RP-HPLC on a Reprosil Gold 200 column by elution with an acetonitrile gradient. The fraction containing ACTR was lyophilized in a SpeedVac concentrator, dissolved in 0.1 M sodium phophate, pH 7.5, and labeled with Alexa Fluor 488 maleimide at a molar ratio of dye to protein of 0.8:1. The reaction mixture was again reduced with β-mercaptoethanol and purified by RP-HPLC on a Reprosil Gold 200 column. The fraction with the singly labeled ACTR was lyophilized in a SpeedVac concentrator,

dissolved in labeling buffer and labeled with a molar excess of Alexa Fluor 594 maleimide. Doubly labeled ACTR was purified by RP-HPLC on a Reprosil Gold 200 column, and the correct mass was confirmed by ESI-MS.

Analogously, the same IDP variants were labeled with a different FRET pair (ATTO 532 and ATTO 647N, Atto-Tec, Germany) whose spectra are shifted towards higher wavelengths where the influence of fluorescent impurities on the transfer efficiency histograms at high PEG concentrations is strongly reduced.

Preparation of crowding solutions. Crowding experiments were carried out in 50 mM sodium phosphate buffer, pH 7.0. Crowding solutions were prepared by mixing acidic (50 mM NaH_2PO_4 + crowding agent) and alkaline (50 mM Na_2HPO_4 + crowding agent) stock solutions to a final pH of 7.0 (+/- 0.2). The concentration of the stock solutions depended on the solubility and purity of the crowding agent used (between 10 % w/w and 40 % w/w crowding agent). Crowding solutions with lower concentrations were prepared by dilution of the corresponding stock solution to the desired concentration with 50 mM sodium phosphate buffer, pH 7.0.

Single-molecule fluorescence spectroscopy. Single-molecule fluorescence measurements were performed with a MicroTime 200 confocal microscope (PicoQuant, Germany) equipped with a diode laser (LDH-D-C-485, PicoQuant, Germany), a 20 MHz supercontinuum laser (SC-450-4, Fianium, UK; wavelength selected with a z582/15 band pass filter (Chroma)) for pulsed interleaved excitation (PIE) (61), and an Olympus UplanApo 60x/1.20W objective (Olympus). Photons emitted from the sample were collected by the same objective. Remaining excitation light was eliminated by a filter (HQ500LP, Chroma Technology) before the emitted photons passed the confocal unit with a 100 μm pinhole. The emitted photons were separated into four channels with a polarizing beam splitter and a dichroic mirror (585DCXR, Chroma). Donor photons were filtered (ET525/50m, Chroma Technology) and then focused on a τ-SPAD avalanche photodiode (PicoQuant). Acceptor photons were filtered (HQ650/100m, Chroma Technology) and detected by a τ-SPAD (PicoQuant). The arrival time of every detected photon was recorded with a HydraHarp 400 counting module (PicoQuant).

All measurements were performed by exciting the donor dye with a laser power of 100 μW at the back aperture of the objective. For PIE measurements, the power used for exciting the acceptor dye was adjusted to match the intensity of the donor emission (between 50 and 70 μW). Single-molecule FRET efficiency histograms were acquired in samples with protein concentrations of about 50 pM to 100 pM. The time between excitation pulse and photon detection was stored with 16 ps resolution, with the lasers pulsed at a repetition rate of 20 MHz. The measurements were performed in 50 mM sodium phosphate buffer, pH 7.0, 200 mM β-mercaptoethanol, and 0.001% Tween-20 with varying concentrations of crowding agents and/or denaturants (guanidinium chloride, urea) or potassium chloride. Each sample was measured for 30 min to 1h at 295 K.

Data Analysis

FRET efficiency histograms. Fluorescence bursts from individual molecules were identified by combining successive photons separated by inter photon times of <100 μs and retaining the burst if the total number of photons detected after donor excitation was >50. Transfer efficiencies for each burst were calculated according to $E=n_A/(n_A+n_D)$, where n_D and n_A are the numbers of donor and acceptor photons, respectively. Corrections for background, acceptor direct excitation, channel crosstalk, differences in detector efficiencies, and quantum yields of the dyes were applied (6). The precision of the measurements as estimated from multiple independent measurements is typically ±0.01 transfer efficiency units and thus comparable to or smaller than

the data points reported in the figures, unless shown explicitly. We estimate a systematic error for R_g of less than ±0.2 nm for the entire dataset. However, a uniform shift of this magnitude for all data toward higher or lower values of R_g does not affect any of our conclusions.

The changes in refractive index caused by increasing concentrations of crowding agents were measured with a digital Abbe refractometer (Krüss, Germany) and were used to recalculate the Förster radius (R_0) for every sample under the assumption that the polymeric crowding agents pervade the solutions uniformly. This assumption does not affect our conclusions, since the narrow range of refractive indices between 1.34 and 1.39 for our experimental conditions has a minor effect on the dimensions of the proteins. Even if we assumed the extreme case that no refractive index change was experienced by the protein locally upon going from pure buffer to the highest volume fraction of PEG, the lack of a refractive index correction would correspond to an apparent compaction of the protein between 0.05 nm (at transfer efficiency of 0.8) and 0.1 nm (at transfer efficiency of 0.3) relative to the values reported here.

Fluorescence lifetimes and anisotropy. Multiparameter detection allows us to exclude possible interfering artifacts, such as insufficient rotational averaging of the fluorophores or quenching of the dyes (62). The dependence of the fluorescence lifetimes on transfer efficiencies determined for each burst (Fig. S5) was compared with the behavior expected for fixed distances and for a chain sampling a broad distribution of distances. For a fixed distance, r, the mean donor lifetime in the presence of acceptor is given by $\tau_{DA}(r) = \tau_D (1-E(r))$, where τ_D is the lifetime in the absence of acceptor, and $E(r) = 1/(1+r^6/R_0^6)$. For a chain with a dye-to-dye distance distribution $P(r)$, the donor lifetime is $\tau_{DA} = \int_0^\infty tI(t)dt / \int_0^\infty I(t)dt$, where $I(t) = I_0 \int_0^\infty P(r)e^{-t/\tau_{DA}(r)}dr$ is the time-resolved fluorescence emission intensity following donor excitation. Donor and acceptor lifetimes at different concentrations of crowding agents were analyzed by fitting subpopulation-specific time-correlated photon counting histograms after donor and acceptor excitation, respectively. This allows us to also examine the dependence of donor and acceptor lifetimes on the solution conditions. A systematic decrease of both donor and acceptor lifetimes of up to 10 % was observed with increasing concentrations of crowding agents. These lifetime changes are consistent with the changes expected according to the Strickler-Berg equation (63) for solutions with different refractive indices. Since the changes in donor and acceptor lifetimes are very similar, the contribution of this effect to the observed transfer efficiencies cancels. The variation of the donor lifetime also has no significant impact on R_0, since the donor quantum yield enters into the calculation of R_0 with the power of 1/6, resulting in a maximum change in R_0 of about 2%, less than the statistical experimental uncertainty.

Subpopulation-specific anisotropies were determined for both donor and acceptor, and values were found to vary between 0.03 and 0.08 for the donor and between 0.11 and 0.18 for the acceptor, consistent with values observed in ensemble measurements, and sufficiently low to assume as a good approximation for the orientational factor $\kappa^2 = 2/3$.

Quantifying the radius of gyration from transfer efficiencies. Essentially as described previously (27), FRET efficiencies are converted to radii of gyration according to

$$E = \int_0^{l_c} E(r) \int_{R_c}^{l_c/2} P(r \mid R_g) P_{FF}(R_g) dR_g dr , \qquad (\text{Eq. S1})$$

where l_c is the contour length, and R_c is the radius of the sphere with volume equivalent to the sum of the volumes V_{aa}^i of all the amino acids, $R_c = \left(\dfrac{3}{4\pi} \sum_i V_{aa}^i \right)^{1/3}$. We use the conditional probability density function for a certain end-to-end distance, r, given the radius of gyration, R_g, suggested by Ziv and Haran (35), which describes the distance distribution of two random points inside the sphere of radius $\sqrt{5} \cdot r_g$ ($\sqrt{5}$ is a scaling factor used to satisfy the condition $6\langle R_g^2 \rangle = \langle r^2 \rangle$),

$$P(r \mid R_g) = \frac{1}{\sqrt{5}R_g} \left[3\left(\frac{r}{\sqrt{5}R_g} \right)^2 - \frac{9}{4}\left(\frac{r}{\sqrt{5}R_g} \right)^3 + \frac{3}{16}\left(\frac{r}{\sqrt{5}R_g} \right)^5 \right], 0 \leq r < 2\sqrt{5}R_g \quad \text{(Eq. S2)}$$

$P_{FF}(R_g)$ is the Flory-Fisk distribution for the radius of gyration

$$P_{FF}(R_g) = Z^{-1} R_g^6 e^{-\frac{7R_g^2}{2\langle R_g^2 \rangle}}, \quad \text{(Eq. S3)}$$

where $\langle R_g^2 \rangle^{1/2}$ is the root-mean-squared radius of gyration of the chain, and Z is the normalization term. In contrast to previous works, we do not apply corrections to the Flory-Fisk distribution introduced by Sanchez theory (35, 64, 65), since the applied weighting proposed by Sanchez would be valid only for the measurements in absence of crowders and would be inconsistent with the other experimental conditions considered here (see *Scaled-particle theory* section). However, using the Sanchez distribution would result only in a systematic shift of all radii of gyration by approximately 0.1-0.2 nm, which does not affect any conclusions of this work.

Scaled-particle theory (SPT). Following the approach proposed by Minton (37), the effect of macromolecular crowding on the unfolded state can be quantified by weighting the probability density function of the radius of gyration of the disordered ensemble, $P(R_g)$, according to the chemical potential, $\Delta\mu = \Delta\mu(\phi, R_g, R_g^{crd})$, obtained with SPT:

$$\langle R_g^2 \rangle = \frac{\int R_g^2 P(R_g) e^{-\frac{\Delta\mu(\phi, R_g, R_g^{crd})}{k_B T}} dR_g}{\int P(R_g) e^{-\frac{\Delta\mu(\phi, R_g, R_g^{crd})}{k_B T}} dR_g}. \quad \text{(Eq. S4)}$$

The simplest choice for $P(R_g)$ is the Flory-Fisk distribution (Eq. S3), where $\langle R_g^2 \rangle^{1/2}$ is substituted by the root-mean-squared radius of gyration of the chain in absence of crowding agents, $\langle R_{g0}^2 \rangle^{1/2}$. If we assume that both the unfolded protein and the crowding agent can be described as rigid spheres (as in the classic SPT), the excess chemical potential of the IDP in the presence of crowding can be written as:

$$\frac{\Delta\mu(\phi, R_g, R_g^{crd})}{k_B T} = -\log(1-\phi) + \left[\overline{R}^3 + 3\overline{R}^2 + 3\overline{R}\right]\frac{\phi}{1-\phi} + \left(2\overline{R}^3 + \frac{9}{2}\overline{R}^2\right)\left(\frac{\phi}{1-\phi}\right)^2 + 3\overline{R}^3\left(\frac{\phi}{1-\phi}\right)^3, \text{ (Eq. S5)}$$

where $\overline{R} = \dfrac{R_g}{R_g^{crd}}$; ϕ is the volume fraction of crowding agent in solution; and R_g^{crd} the radius of gyration of the crowder. Consequently, an increase in ϕ or R_g lead to an increase in the excess chemical potential, whereas an increase in R_g^{crd} causes a decrease in the excess chemical potential. Data reported in Fig. 2e are fitted globally to Eqs. S4 and S5 with a different $\langle R_{g0}^2 \rangle^{1/2}$ for each IDP and a single effective R_g^{crd} as an adjustable parameter shared by all four proteins (Fig. S6).

A modification of the classic SPT suggested by Minton (37) allows the polymeric nature of the IDP to be taken into account within the SPT framework. Here the unfolded state is represented as a Gaussian cloud where the average number density of residues can be described as a function of the distance from the center of the mass of the protein, r_p, as

$$\rho(r_p) = n\frac{3}{2\pi\langle R_g^2 \rangle^{1/2}}e^{-\frac{3r_p^2}{2\langle R_g^2 \rangle}} \qquad \text{(Eq. S6)}$$

For a system consisting of the protein and a single sphere in solution, r_p can be expressed in terms of the distance between the centers of mass of the two objects, r_{sep}, and the radius of the sphere, which in this case is the radius of the crowding agent, R_g^{crd} (see Fig. S3). The probability, P_0, that no chain segments of the IDP lie within the volume of an arbitrarily placed hard sphere is calculated as a function of R_g of the IDP,

$$\log P_0 = -\left(\frac{6}{\pi}\right)^{1/2}\frac{n}{R_g r_{sep}}e^{-\frac{3r_{sep}^2}{2R_g^2}}\int_0^{R_g^{crd}}e^{-\frac{3r^2}{2R_g^2}}\sinh\frac{3r_{sep}r}{R_g^2}rdr. \qquad \text{(Eq. S7)}$$

Rescaling all distances relative to the size of the crowding agent, R_g^{crd}, yields

$$r_{sep} = f_{sep}R_g^{crd} \qquad \text{(Eq. S8)}$$

$$R_g = f_g R_g^{crd} \qquad \text{(Eq. S9)}$$

$$r = xR_g^{crd}. \qquad \text{(Eq. S10)}$$

P_0 can be written in terms of the rescaled dimensions as

$$\log P_0 = -\left(\frac{6}{\pi}\right)^{1/2}\frac{n}{f_g f_{sep}}e^{-\frac{3f_{sep}^2}{2f_g^2}}\int_0^1 e^{-\frac{3x^2}{2f_g^2}}\sinh\frac{3f_{sep}x}{f_g^2}xdx. \qquad \text{(Eq. S11)}$$

By equating the co-volume of the Gaussian cloud and the crowding agent with the co-volume of two hard spheres, an equivalent effective hard-sphere radius, R_g^{eff}, is obtained for each R_g sampled by the IDP, leading to

$$\overline{R}^{eff} = \frac{R_g^{eff}}{R_g^{crd}} = 3\int_0^\infty \left(\left(1 - P_0\left(f_{sep}\right)\right) f_{sep}^2 df_{sep} \right)^{1/3} - 1 \qquad \text{(Eq. S12)}$$

This rescaled $\overline{R}^{eff}$ can then be inserted in Eq. S5 (Fig. S7).

Further extensions of SPT. In efforts to go beyond the simple description of a fluid of hard spheres, different extensions of the SPT have been implemented. SPT equations have been revised to account for ellipsoidal, cylindrical and infinite rod-like particles (37, 66-68). None of these corrections for different shapes can account for the trends observed in our experimental results. More recently, Qin and Zhou (69) have approached the problem of crowding on IDPs by calculating the co-volume on the basis of explicit simulations of the disordered protein and of the crowding agent in isolation. Even though this post-processing approach captures the effects induced by compact crowders on disordered proteins in their simulations, an extension of this method to polymeric expanded crowders as those used in our experiments has not yet been implemented. Complications in applying this approach come from the difficulty of calculating the correct co-volume between two disordered systems as well as taking into account the change in volume of the polymeric crowder at high concentrations (see the discussion about semidilute regime in the section *Flory-Huggins theories*).

To account for interactions between the crowders and the protein (47), attractive free energy terms have been included in SPT (46, 48), which resulted in the successful description of simulated data (48). A similar approach can be implemented here by adding an attractive interaction between IDP and crowder in Eq. S4. However, even with the functional form suggested by Kim & Mittal (48), the energy parameter would need to be different for each polymer length and possibly for different concentrations to obtain a quantitative fit of our data.

Flory-Huggins theories. A single polymer chain in good solvent adopts swollen conformations and follows a scaling exponent of 3/5, i.e. $R_g^{crd} \sim P^{3/5}$, where P is the number of Kuhn segments of the polymer. Three different concentration regimes need to be distinguished for a polymer in solution: the dilute regime, where the polymer chains are not overlapping; a semidilute regime, where the chains start to overlap and entangle; and a dense regime, where the chains are highly packed (Fig. S1 inset). ϕ^* is the overlap concentration, which separates the semidilute from the dilute regime. ϕ^* can be defined as the concentration of polymer where the volume fraction of the polymer chains in solution is equal to the volume fraction of a single polymer chain, i.e.

$$\phi^* = \frac{Pb^3}{P^{9/5}b^3} = P^{-4/5} . \qquad \text{(Eq. S13)}$$

Flory argued that in concentrated solutions and melts, the polymers exhibit the length scaling of an ideal chain ($R \sim P^{1/2}$) (70). Let us consider the case of one long chain with N segments (the IDP) in a polymer melt of shorter chains with P segments (the crowder). For simplicity, the segment length, b, is assumed to be equal for N-chain and P-chains. By equating the chemical

potentials of crowders inside and outside the volume pervaded by the long chain, a relation between the end-to-end distance, R, of the long N-chain and the number of segments of the P-chains can be obtained (39):

$$\frac{R}{Nb^2} - \frac{N^2 b^3}{PR^4} - \frac{1}{R} = 0$$

(Eq. S14)

If $P << N$, the third term in the equation can be neglected, and the size of the long chain can be described by the equation

$$R = N^{3/5} P^{-1/5} b.$$

(Eq. S15)

In the case of large P, the second term in Eq. S14 can be neglected, and ideal scaling is recovered:

$$R = N^{1/2} b.$$

(Eq. S16)

The crossover between small and large P is determined by equating Eqs. S15 and S16, which results in the threshold given by the Flory criterion: $P = N^{1/2}$ (39).

In our experiments, we investigate a **ternary system** composed of
- individual test chains with N segments (the IDP),
- a volume fraction, ϕ, of polymer chains with P segments (the crowding agent),
- and the solvent.

Similar to the case of the polymer melt (39), it is possible to describe the interaction between the long chain (the IDP) and the other polymers (the crowding agent) in terms of an effective medium interaction parameter. This term is obtained in the mean field approach of Joanny et al. (39) by equating the chemical potentials of the short chains (crowders) inside and outside the long chain (IDP). The effective medium interaction parameter is then given by:

$$u = \frac{1}{1 + P\phi}$$

(Eq. S17)

To study the effects of the crowder concentration on the size of the IDP, it is helpful to treat the IDP as a sequence of blobs of size R_P. In dilute solution, on length scales smaller than R_P, the N-chain behaves in the same way as the P-chains, whereas on length scales greater than R_P, the ternary properties of the system become relevant. In the latter case, the long chain formed by N/P blobs experiences the effective medium interaction that in rescaled units is (39)

$$u = \frac{1}{1 + \phi/\phi^*}.$$

(Eq. S18)

For a chain in good solvent, the radius of gyration is

$$R_g = bN^{3/5} u^{1/5}$$

(Eq. S19)

And thus, in blob-rescaled units,

7

$$R_g = R_g^{crd} \left(\frac{N}{P} \right)^{3/5} \left(\frac{1}{1+\phi/\phi^*} \right)^{1/5} = R_{g0} \left(\frac{1}{1+\phi/\phi^*} \right)^{1/5} \qquad \text{(Eq. S20)}$$

The equation can be further extended to the semidilute regime (45). However, since this theory is only valid for the case of a long chain in a solution of shorter chains, this regime will only be approached marginally in our experiments.

For the data analysis presented in Figs. 3 and 4, we modified Eq. S20 by introducing a fitting parameter a, similar to the effective interaction term proposed by Nose (45):

$$R_g = R_{g0} \left(\frac{1}{1+a\phi/\phi^*} \right)^{1/5} \qquad \text{(Eq. 1a, see main text)}$$

All other parameters are not adjustable: ϕ^* is given by Eq. S13, and R_{g0} is obtained from the radius of gyration of each protein in the absence of crowding. a corresponds to a correction of the effective medium interaction term in Eq. S17, which is calculated for a very long chain in a bath of shorter chains, where the long chain is in good solvent and assumed to be large enough to accommodate the small chains (Fig. S8). The degree of expansion of the IDPs investigated here depends on their specific sequence (27), resulting in differences in the interaction term. The values of a obtained from the fits reflect the expected trend and exhibit an increasing deviation from $a = 1$ with increasing compactness of the protein (Table S4).

Extending the classical Flory-Huggins theory to the case of $P > N^{1/2}$ requires a realistic estimate of the density fluctuations in the solution when the solution is no longer dilute. A corresponding quantitative description is provided by the renormalized Flory-Huggins theory derived by Schäfer and Kappeler (44). Renormalization group theory establishes equivalence between microscopically different systems through scaling laws. In doing so, it allows to map a system of long chains (where common perturbation theories break down) onto a system of effectively short chains (where perturbation theories hold).

Here we introduce a length l_0, which defines a sort of lattice unit for the system and will be used to describe both the N-chain (the IDP) and the P-chains (the crowding agent). Following the treatment of Schäfer, we set l_0 equal to the length of the Kuhn segment of the N-chain. Here we adopted the same l_0 for all four proteins, according to the value obtained for ProTα. All the other chemical differences in structure and flexibility between the two chains will be absorbed in specific parameters. The renormalization is then introduced via a renormalized length, $l_R = l_0/\lambda$, where $\lambda < 1$. Similarly, the number of segments of each chain and the volume fraction are rescaled as a function of the same λ parameter:

$$N \rightarrow N_R(\lambda) \qquad \text{(Eq. S21a)}$$

$$P \rightarrow P_R(\lambda) \qquad \text{(Eq. S21b)}$$

$$\phi \rightarrow \phi_R(\lambda). \qquad \text{(Eq. S21c)}$$

The connection between the microscopic information and the renormalized parameter is given by:

$$1 = \frac{1}{N_R} + 2\left(\hat{u}B_N\phi l_0^{-3}N^{1.76} + \hat{u}\left(\frac{B_P}{B_N}\right)^{\frac{1}{0.588}} B_N^3\phi l_0^{-3}N^{0.76}\right)N^{-0.76}, \qquad \text{(Eq. S22)}$$

where $\hat{u} = 5.756$ is a parameter connected to the overlap probability of chains in the semidilute regime; $B_i = \frac{R_{g0}^{(i)}}{0.8^{0.5}i^{0.588}}$, with $i = \{P, N\}$, contains the structural details of the single N- and P-chains in highly dilute solutions under the assumption that both N- and P-chains are in good solvent; and λ is chosen in order that $l_R = B_N\left(\frac{N}{N_R}\right)^{0.588}$. The radius of gyration is then given by

$$R_g(N, P, \phi, s_{NP}) = l_R^2 N_R\left\{0.636 + 0.165N_R^{1/2} - 0.292N_R^{1/2}f_{NP}^2 G(\phi_R P_R, \frac{N_R}{P_R})\right\} \qquad \text{(Eq. S23)}$$

where $G(W, y) = W\int_0^\infty z^{-1/2}\frac{B(z)D(zy)}{1 + WD(zy)}dz$ is formally similar to the result obtained with the uniform expansion model (71) when the expansions due to the renormalization are condensed in terms of

$$B(z) = \frac{1}{6}e^{-z} - 2D(z) - \frac{8}{z}(D(z) - 1) - \frac{10}{z^2}(D(z) - 1 + \frac{z}{3}) \qquad \text{(Eq. S24)}$$

$$D(z) = \frac{2}{z^2}(e^{-z} - 1 + z). \qquad \text{(Eq. S25)}$$

The term f_{NP} is obtained under the assumption that interactions between N- and P-chains are small (44), leading to the equation $f_{NP}(s_{NP}) = 1 + \left(\frac{l_R}{s_{NP}}\right)^{-0.40}$, where s_{NP} is an invariant parameter with the dimensions of a length that quantifies the interactions between the N- and P-chains. f_{NP} can be connected to the Flory interaction parameter, χ, through the equation $|\chi| = |1 - f_{NP}|$. However, the parameter s_{NP} is preferred to χ since the latter is not invariant in the renormalization flow.

Note that in the global fit of the radii of gyration as a function of volume fraction of PEG for all IDPs (Fig. 3) with the renormalized Flory-Huggins theory (Fig. S9), the only adjustable parameter is s_{NP}, which is taken to be identical for all PEG sizes, but allowed to vary from protein to protein (Table S4); B_N and B_P are well-defined by experimental observables: B_N is calculated from the radius of gyration measured for each protein in the absence of crowding and B_P from the reported values of the radii of gyration for PEG (see Fig. S1 and *PEG scaling law*). If s_{NP} is close to zero, protein and crowding agent are indistinguishable in terms of inter- and intramolecular interactions. In Fig. S4a, the robustness of the functional form of the fitting function at different values of the fitting parameter s_{NP} is illustrated.

s_{NP} provides a new opportunity to quantify the interactions between protein and crowder beyond simple excluded volume effects, sometimes referred to as "chemical interactions". The two variants of ProTα are well fitted with almost identical values of s_{NP} (see Table S4), whereas slightly different values were obtained for ACTR and IN, indicating small variations in the

interactions between PEG and proteins. The values obtained are of the same order of magnitude as those previously reported in the literature for ternary solutions of synthetic polymers (72). A conversion of s_{NP} to the more intuitive parameter χ yields repulsive interactions in the range of 0.1-0.3 $k_B T$ per segment between PEG and ProTα or ACTR. Interestingly, the fitted values for the experiments with ProTα and other polymers (see Table S5) suggest lower or even undetectable chemical interactions between the protein and the polymers. The contribution to the overall effects observed here is small (Fig. S4), but this trend is consistent with previous suggestions that PEG may be less inert than other polymers commonly employed in crowding experiments (13). One of the strengths of the approach presented here is the possibility to model a complex polymeric solution including such repulsive (or attractive) interactions.

In the application of the Flory-Huggins theories, we have approximated the length of a Kuhn segment by 0.76 nm for both protein and PEG according to previously reported persistence lengths (27, 73), which is equivalent to two bond segments. Consequently, the number of Kuhn segments of the N- and P-chains is given by half the degree of polymerization. In the case of PEG, the concentration in weight fraction was converted to volume fraction according to $\phi_{v/v} = \phi_{w/w} / (\rho(1-\phi_{w/w}) + \phi_{w/w})$ where $\rho = 1.12$ g/cm^3 is an average density for pure solutions of short PEGs. This approach is justified since no significant volume contraction is reported for solutions with the PEG concentrations used here. For the other crowding agents, where specific densities in solution were not reported, a direct correspondence between volume and weight fraction based on the densities of the pure substances was assumed.

PEG scaling law. According to Devanand *et al.* (29), water is a good solvent for PEG. Fig. S1 shows the scaling law obtained in (29) for long PEGs with the radii of gyration of PEGs used in the current study. The radii of gyration of PEGs are taken from (74, 75). In cases where only the hydrodynamic radius was determined experimentally, a conversion between hydrodynamic radius and radius of gyration was applied according to the ratio determined experimentally in (29). A deviation from the predicted scaling behavior (29) is visible for short PEGs, for which finite length effects start to dominate.

Estimation of the radius of gyration of IDPs at the Θ-state. An estimate of the radius of gyration for the four proteins in Θ-state conditions is obtained according to the previous analysis of the scaling exponent of disordered and unfolded sequences presented by Hofmann *et al.* (27), where the radius of gyration is linked to the scaling exponent by (76)

$$R_{g\Theta} = \sqrt{\frac{2l_p^* b}{(2\nu+1)(2\nu+2)}} N^\nu, \qquad \text{(Eq. S26)}$$

where l_p^* = 0.4 nm, $b = 0.38$nm, $\nu = 0.5$, and N is the number of amino acids of the respective protein. The resulting radii of gyration in Θ-solvent are about 1.7 nm for IN, 1.8 nm for ProTα−C and ProTα−N, and 2 nm for ACTR.

Estimation of scaling exponents of IDPs. Following the empirical relation for the scaling exponent as a function of the hydrophobicity and net charge of unfolded and disordered proteins obtained previously (27), we estimated the scaling exponent for all full-length disordered sequences longer than 25 amino acids deposited in the Disprot database (v6.01) (77).The exponent ν is calculated according to

$$v(Q) = 1/3 + a\left[1 + \exp(x_0 - Q)/z\right]^{-1} \text{ and } v(H) = 1/3 + a\left[1 + \exp(x_0 + cH - d)/z\right]^{-1}, \quad \text{(Eq. S27)}$$

where H is the hydrophobicity according to the scale of Kyte and Doolittle (78), Q is the mean net charge of the sequence, $a = 0.394$, $z = 0.09$, $x_0 = 0.114$, $c = 1.72$ and $d = 0.9$.
The exponent is determined according to

$$v = \begin{cases} v(Q) & u^* > 0 \vee f = 0 \vee g = 0 \\ v(H) & u^* \le 0 \vee f = 0 \wedge g = 0 \end{cases}, \quad \text{(Eq. S28)}$$

where f and g are the fractions of positive and negative charges in the sequence, respectively, and u^* is calculated according polyampholyte theory (11) as

$$u^* = \frac{4\pi l_b (f-g)^2}{\kappa^2} - \frac{\pi l_b^2 (f+g)^2}{\kappa}, \quad \text{(Eq. S29)}$$

where l_b is the Bjerrum length, and κ^{-1} is the Debye length.

We note that a higher percentage of globule-like IDPs has been estimated from simulations for a different subset of the Disprot database (33, 34). However, taking into account polyampholyte effects and patterning, it has been predicted that the majority of IDPs will maintain coil-like properties (34), and consequently they should be susceptible to the effect of crowding described here.

Physiological concentrations of IDPs in the nuclear pore complex and in RNA granules. A nuclear pore complex contains approximately 200 disordered nucleoporins containing FG-repeats, each with a length of ~600 amino acids (79, 80). From the chain length of these sequences, the overlap concentrations can be estimated to be in the range between of volume fractions between 0.05% and 4%. Assuming the nuclear pore to have a diameter of 30 nm and a height of 40 to 80 nm (25, 80, 81), the volume fraction occupied by the disordered nucleoporins is easily estimated as $\phi_{NP} = \dfrac{v_{NP}}{V_{pore}} = \dfrac{n_{NP} \cdot N_{NP} \cdot \langle v_{aa} \rangle}{\pi r_{pore}^2 h_{pore}}$, where v_{NP} is the volume occupied by the nucleoporins; V_{pore} is the volume available in the pore; n_{NP} is the number of nucleoporins; N_{NP} is the sequence length of nucleoporins; $\langle v_{aa} \rangle$ is the average volume of the amino acid residues (approximately 0.13 nm³); r_{pore} and h_{pore} are, respectively, the radius and the height of the pore. The volume fraction occupied by disordered nucleoporins is therefore between 25 and 55%, about an order of magnitude higher than the overlap concentration. The effects discussed in the main text are thus highly likely to be of importance for the conformational distributions of nucleoporins *in vivo*.

Various IDPs have been identified in RNA granules (22, 82, 83). Recent work has shown that the multivalency of these proteins can control phase separation and therefore the assembly of RNA granules (23). Even though the mechanism is not fully understood, and the proteins can undergo different conformational changes during the phase-separation process, the mechanism suggested by Li et al. (23) can be taken as an example to test whether the polymeric nature of the proteins is expected to be important in that range of concentrations. For the case of the engineered proline-rich motives (PRM) (23), the sequence is likely to be almost completely disordered. The molar concentration of the protein at which a given volume is occupied entirely by those IDPs is given by $c = 1/(N \langle v_{aa} \rangle \cdot N_A)$, where N is the number of amino acids of the sequence, and N_A is the Avogadro number. A calculation for the case of a sequence with 250 amino acids as those

considered in the work of Li *et al. (23)* result in a local protein concentration in the range of ~50 mM. The corresponding overlap concentration is estimated to be between volume fractions of 1% and 6% or 0.5 and 3 mM. Considering that two different proteins are mixed in similar ratios in these experiments, a concentration of 0.25 to 1.5 mM is sufficient to reach the overlap regime. Phase separation for proteins of this length occurs at concentrations of approximately 50 µM, only 5 times less than the overlap concentration. However, due to phase separation, in the droplets, a concentration of proteins 100 times higher than the bulk solution is reported (23). The confinement in the droplet is therefore plausibly causing an increase of protein concentration significantly higher than the overlap concentration, and the overlap between disordered coils will affect the conformations of the disordered sequences. FUS and hnRNPA2, two disordered proteins identified in RNA granules, have been shown to exhibit a sol-gel transition *in vitro* (82) at a concentration above 1 mM with an overlap concentration ranging between 0.15 and 1 mM. Therefore, these proteins are expected to be in the semidilute regime before gelation.
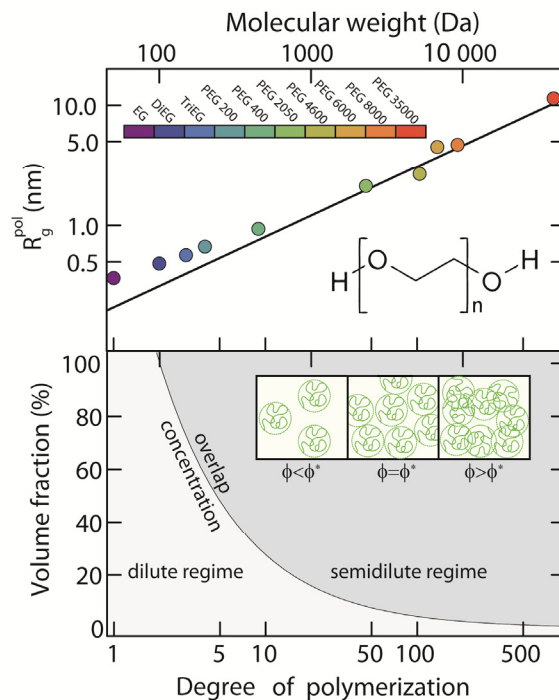
Figure S1. Polymer properties of polyethylene glycol. (a) Radius of gyration of PEG as a function of molecular weight/degree of polymerization (74, 75) with a fit (black line) to the scaling law $R_g^{pol} = 0.21\,\text{nm} \cdot P^{0.583}$ (26). The scaling exponent indicates that water is a good solvent for PEG. Deviations from the fit (which was obtained for PEG molecules over the entire range of lengths originally reported (29)) are due to finite length effects for small values of P. (b) Overlap concentration as obtained from Eq. S10, and schematic representation of a polymer solution in the dilute regime, at the overlap concentration, and in the semidilute regime.
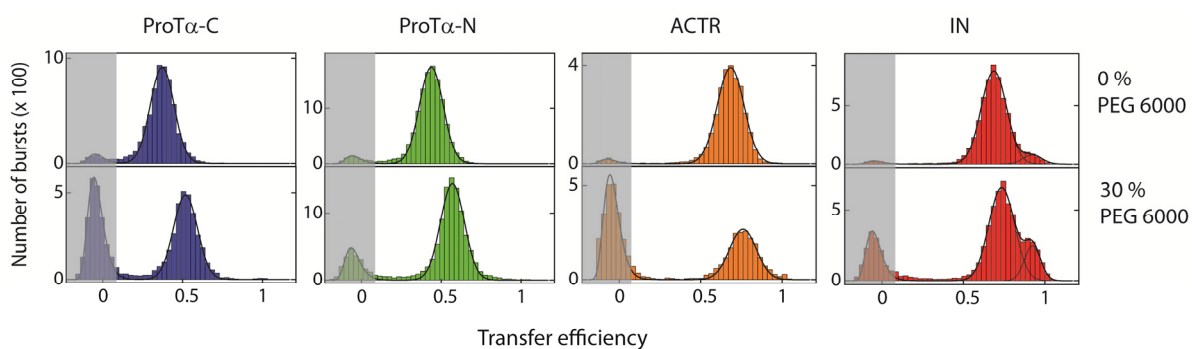
Figure S2. FRET efficiency histograms obtained with FRET dyes shifted toward longer wavelengths compared to Fig. 2. Histograms for ProTα-C, ProTα-N, ACTR, and IN variants labeled with ATTO546 and ATTO647N in the absence and presence of high PEG concentration. The shift towards higher excitation and emission wavelengths reduces the contribution of fluorescence background from impurities in the PEG and provides additional evidence that the peak broadening at high PEG concentration observed in Fig. 2 is mainly due to impurities in the solution. Only in the case of IN, a second peak corresponding to the folded state is detected, consistent with the observations and data analysis in Fig. 2. Gaussian and lognormal distributions were used to fit the peaks (solid lines). The donor-only peaks originating from molecules lacking an active acceptor dye are shaded in grey.
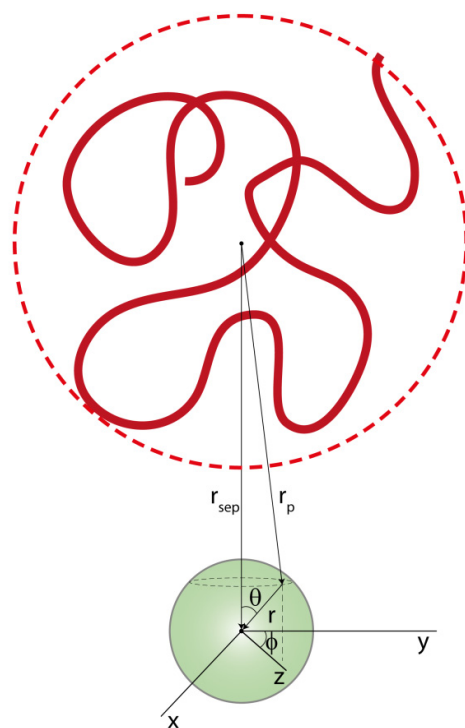
Figure S3. Gaussian cloud model. Representation of the Gaussian Cloud with a disordered conformation of the protein (in red), with the center of mass positioned at distance r_{sep} from a hard sphere (in green) with radius r. Adapted from (37).
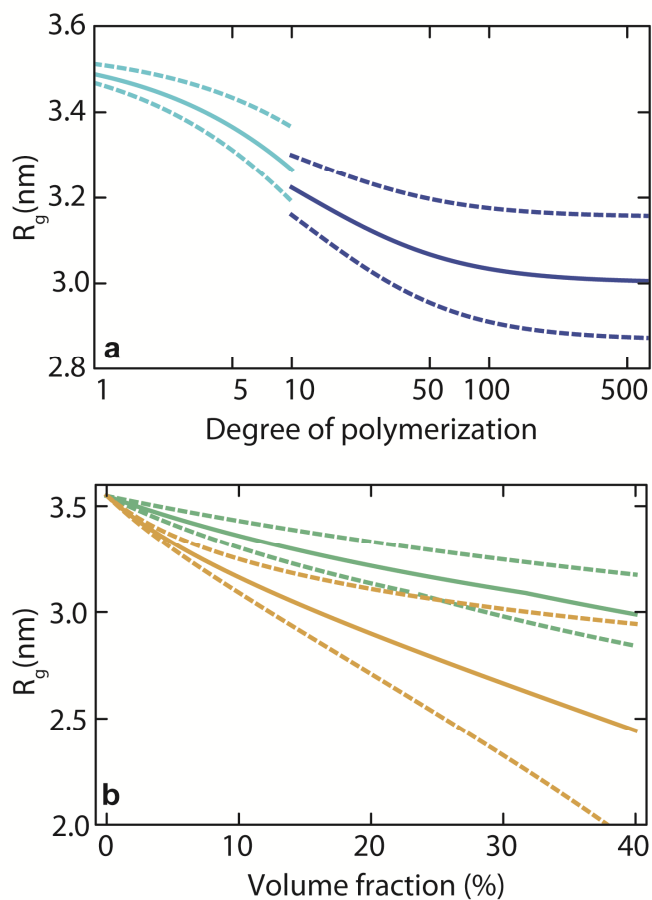
Figure S4. Effects of model parameters in the Flory-Huggins theories. Upper panel: Calculated radius of gyration of ProTα-C as a function of the degree of polymerization of PEG at a volume fraction of 15% according to Flory-Huggins theory (cyan) and renormalized Flory-Huggins theory (blue). Dashed curves show the change in the prediction of Flory-Huggins theory if a deviation of ±50% from the fitted value for the parameter *a* is assumed, and the response of renormalized Flory-Huggins theory to the fitting parameter s_{NP} between 0 (no interactions) and the upper limit of 0.1 nm (strong interactions). Lower Panel: estimation of the radius of gyration of ProTα-C at different volume fractions for PEG 400 (green solid curve) and PEG 6000 (yellow curve). Dashed lines report the response to the fitting parameter of the Flory-Huggins theory for PEG 400 and of the renormalized Flory-Huggins theory for PEG 6000 at the same conditions described above.
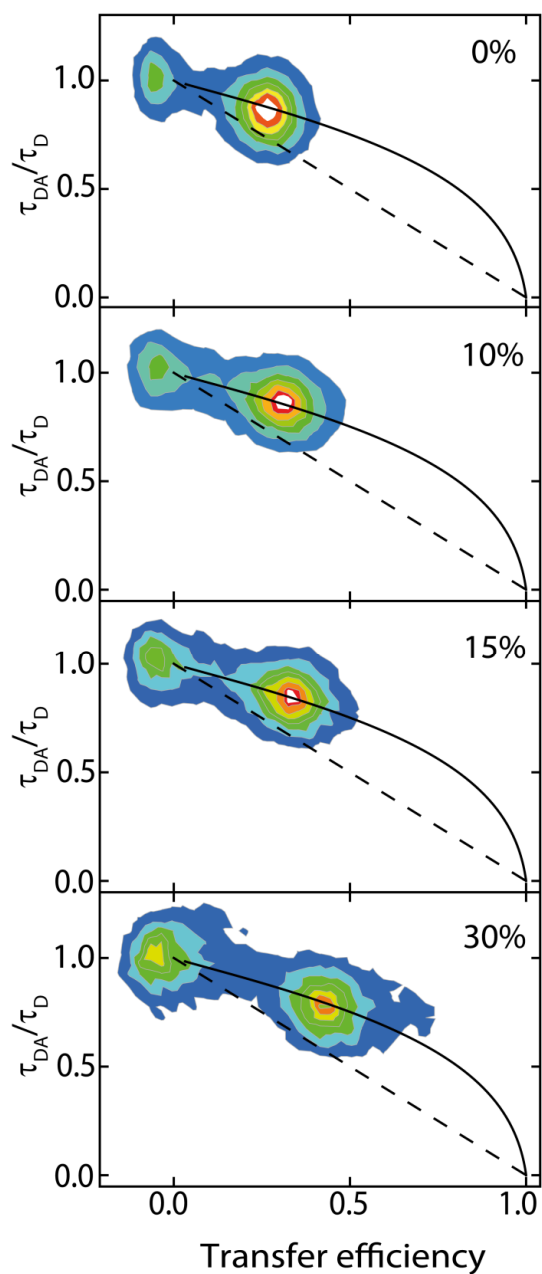
Figure S5. Multiparameter single-molecule fluorescence analysis. Two-dimensional histograms of relative donor τ_{DA}/τ_D lifetime versus FRET efficiency measured between 0 and 30% volume fraction of PEG 6000 compared to the expected trend for a fixed distance (black dashed line) and for a chain reconfiguring over the distribution of distances *P(r)* given by Eq. S2 (black solid line), as described in detail in the section *Fluorescence lifetimes and anisotropies*.

Scaled Particle Theory

from experimental data

$R_{g0}^{(N)}$

ϕ

fit parameter

$R_{g0}^{(P)}$

calculate $P(R_g)$ according to Eq. S3

calculate $\Delta\mu$ according to Eq. S6
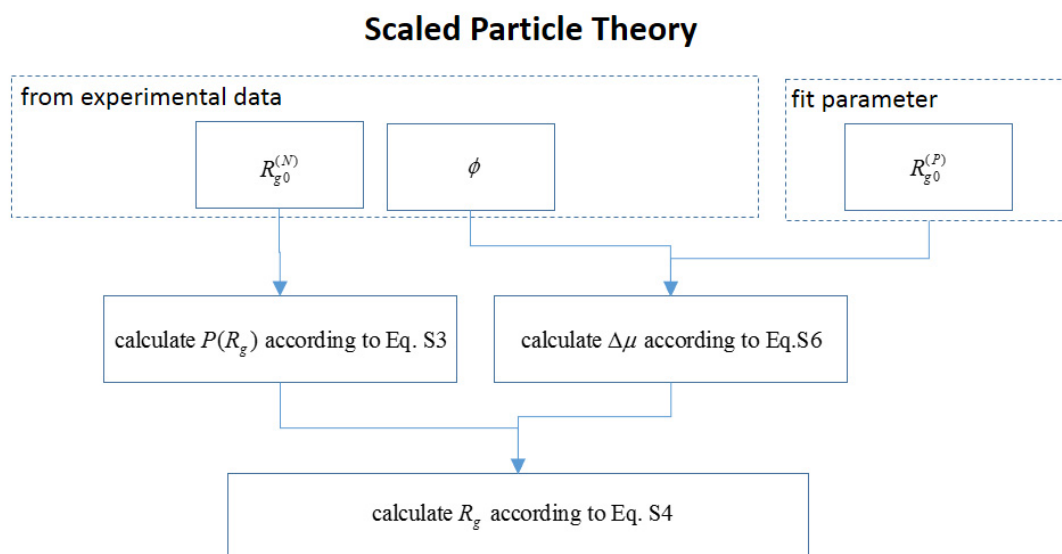
calculate R_g according to Eq. S4

Figure S6. Flowchart for the fitting procedure with scaled-particle theory
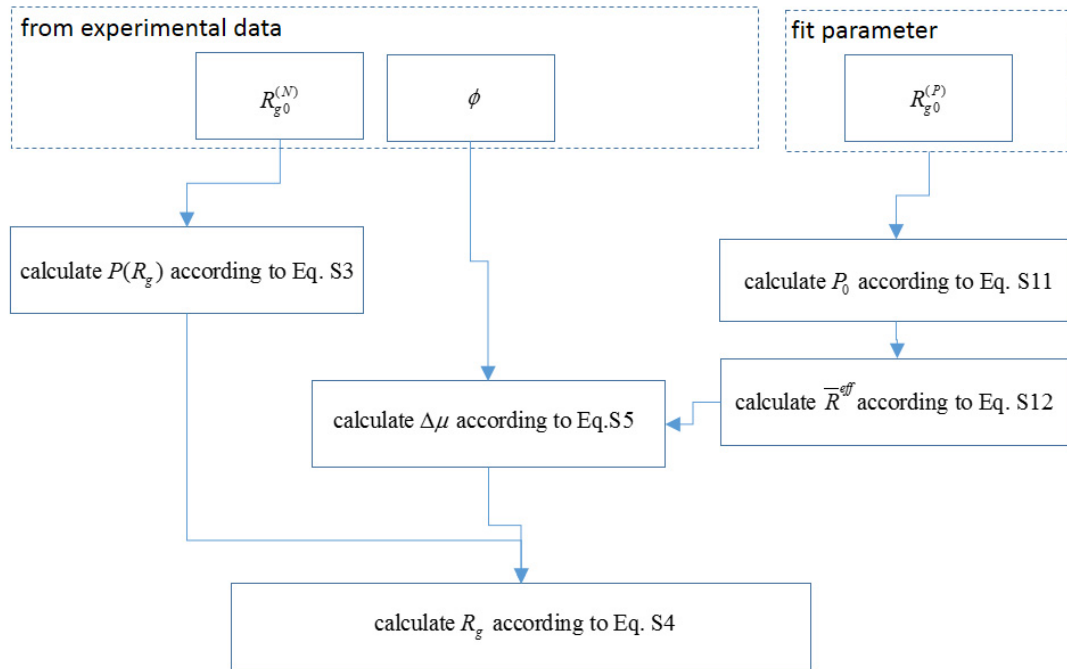
Gaussian Cloud model

Figure S7. Flowchart for the fitting procedure with the Gaussian cloud model
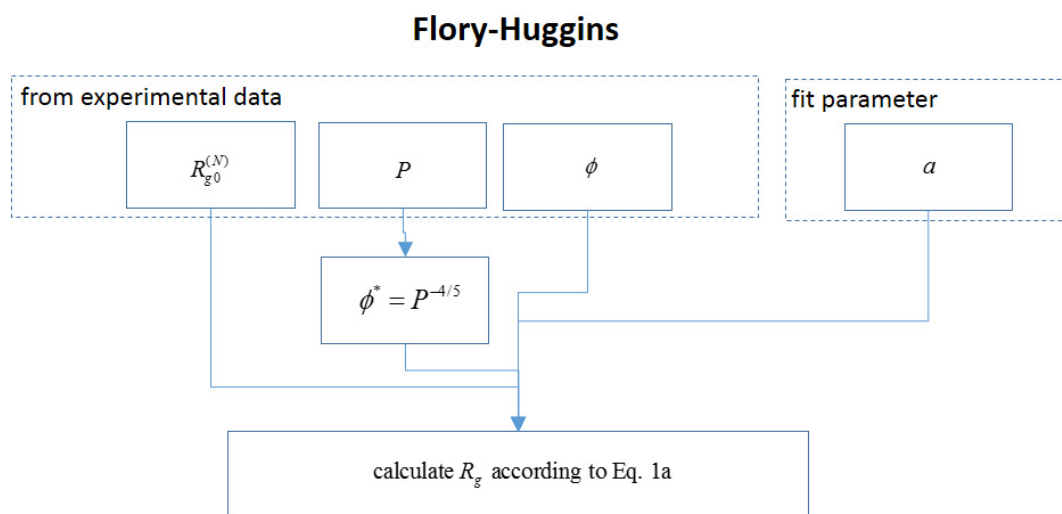
Flory-Huggins

Figure S8. Flowchart for the fitting procedure with Flory-Huggins theory.

Renormalized Flory-Huggins

from experimental data

l_0

$R_{g0}^{(N)}, N$

$R_{g0}^{(P)}, P$

ϕ

fit parameter

s_{NP}

$$B_N = \frac{R_{g0}^{(N)}}{0.8^{0.5} N^{0.588}}$$

$$B_P = \frac{R_{g0}^{(P)}}{0.8^{0.5} P^{0.588}}$$

calculate N_R according to Eq. S22

calculate $l_R = B_N \left(\dfrac{N}{N_R} \right)^{0.588}$

$$f_{NP} = 1 + \left(\frac{l_R}{s_{NP}} \right)^{-0.4}$$

calculate R_g according to Eq. S23

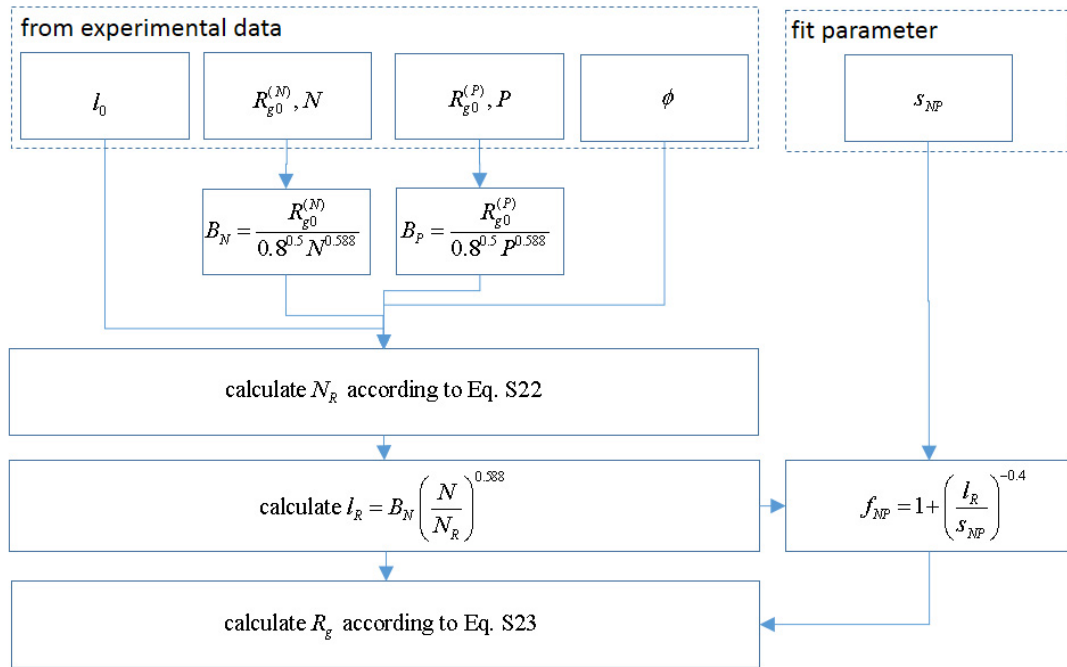**Figure S9.** Flowchart for the fitting procedure with the renormalized Flory-Huggins theory.

	Mol. Weight (Da)	Average degree of polymerization
Ethylene glycol[*]	62.07	1
Diethylene glycol[*]	106.12	2
Triethylene glycol[*]	150.17	3
Polyethylene glycol 200[*]	190 - 210	4
Polyethylene glycol 400[*]	380 - 420	9
Polyethylene glycol 2050[*]	1900 - 2200	46
Polyethylene glycol 4600[*]	4400 - 4800	104
Polyethylene glycol 6000[*]	5000 - 7000	136
Polyethylene glycol 8000[Error! Bookmark not defined.]	7300 - 9000	185
Polyethylene glycol 35'000[*]	35000	795
Polyvinyl alcohol 10'000[*]	9000 - 10000	216
Polyvinyl alcohol 40'000[*]	31000 - 50000	920
Polyvinyl alcohol 90'000[*]	89000 - 98000	2125
Polyvinylpyrrolidone K90[*]	360000	3243
Polyvinylpyrrolidone 1.3M[*]	1300000	11712
Dextran 6000[*]	6000	37
Dextran 40'000[*]	40000	247
Dextran 100'000[*]	100000	617

[*]Sigma-Aldrich (Switzerland), [Error! Bookmark not defined.]Carl Roth (Germany)

Table S1. Crowding agents used in this study.

	1	10	20	30	40	50	56	60	70	80	90	100
ProTα-C (C56-C110)	GP	SDAAVDTSSE	ITTKDLKEKK	EVVEEAENGR	DAPANGNAEN	EENGEQEADN	EVDEE**C**EEGG	EEEEEEEEGD	GEEEDGDEDE	EAESATGKRA	AEDDEDDDVD
	110											
	TKKQKTDED**C**											
ProTα-N (C2-C56)	GP	**C**DAAVDTSSE	ITTKDLKEKK	EVVEEAENGR	DAPANGNAEN	EENGEQEADN	EVDEE**C**EEGG	EEEEEEEEGD	GEEEDGDEDE	EAESATGKRA	AEDDEDDDVD
	110											
	TKKQKTDEDD											
ACTR (C1-C73)	GP	**C**GTQNRPLLR	NSLDDLVGPP	SNLEGQSDER	ALLDQLHTLL	SNTDATGLEE	IDRALGIPEL	VNQGQALEPK	QD**C** 73			
IN (C8-C57)	GSH	MFLDGID**C**AQ	EEHEKAHSNF	RAMASDFNLP	PVVAKEIVAS	CDKCQLKGEA	MHGQVD**C** 57					

Table S2. Sequences of the proteins used in this study.

	ProTα-C	ProTα-N	ACTR	IN
R_{g0} (nm)	3.46±0.02	3.03±0.02	2.47±0.02	1.95±0.02

	PEG 6000
$R_g{}^{crd}$ (nm)	5.8±0.1

Table S3. Global fit of PEG 6000 data with scaled-particle theory. Parameters obtained from fitting the data in Fig. 2 with Eq. S4

	$P < N^{1/2}$	$P > N^{1/2}$
	a	s_{NP} (nm)
ProTα-C	1.18±0.05	0.032±0.004
ProTα-N	0.7±0.1	0.024±0.008
ACTR	0.8±0.1	0.08±0.02
IN	0.05±0.02	$< 2 \cdot 10^{-6}$ [*]

[*] s_{NP} is sufficiently close to zero that the ternary system reduces to a binary system where the protein and the crowding agents cannot be distinguished

Table S4. Global fit of Protα-C, Protα-N, ACTR and IN in the presence of PEG with Flory-Huggins theories. Parameters obtained from fitting the complete dataset in Fig. 3 with Eqs. 1a and 1b.

	s_{NP} (nm)
PEG	0.032±0.004
PVA	< 4·10^{-5} (*)
PVP	< 4·10^{-6} (*)
Dextran	< 3·10^{-5} (*)

(*)s_{NP} is sufficiently close to zero that the ternary system reduces to a binary system where the protein and the crowding agents cannot be distinguished

Table S5. Fit results with Flory-Huggins theories of ProTα-C collapse in presence of PVA, PVP and Dextran. Parameters obtained from fitting the datasets of ProTα-C in the presence of PEG (Fig. 3), PVA, PVP and Dextran (Fig. 5) with Eq. 1b.

Supporting Information references

1. Dyson HJ & Wright PE (2005) Intrinsically unstructured proteins and their functions. *Nat. Rev. Mol. Cell Biol.* 6(3):197-208.
2. Dunker AK, Silman I, Uversky VN, & Sussman JL (2008) Function and structure of inherently disordered proteins. *Curr Opin Struct Biol* 18(6):756-764.
3. Jensen MR, Ruigrok RW, & Blackledge M (2013) Describing intrinsically disordered proteins at atomic resolution by NMR. *Curr. Opin. Struct. Biol.*
4. Wright PE & Dyson HJ (2009) Linking folding and binding. *Curr. Opin. Struct. Biol.*
5. Ferreon AC, Moran CR, Gambin Y, & Deniz AA (2010) Single-molecule fluorescence studies of intrinsically disordered proteins. *Methods in enzymology* 472:179-204.
6. Schuler B, Müller-Späth S, Soranno A, & Nettels D (2012) Application of confocal single-molecule FRET to intrinsically disordered proteins. *Methods Mol. Biol.* 896:21-45.
7. Ferreon AC, Ferreon JC, Wright PE, & Deniz AA (2013) Modulation of allostery by protein intrinsic disorder. *Nature* 498(7454):390-394.
8. Mao AH, Lyle N, & Pappu RV (2013) Describing sequence-ensemble relationships for intrinsically disordered proteins. *Biochem J* 449(2):307-318.
9. Lyle N, Das RK, & Pappu RV (2013) A quantitative measure for protein conformational heterogeneity. *J. Chem. Phys.* 139(12).
10. Fisher CK & Stultz CM (2011) Protein Structure along the Order-Disorder Continuum. *J. Am. Chem. Soc.* 133(26):10022-10025.
11. Müller-Späth S*, et al.* (2010) Charge interactions can dominate the dimensions of intrinsically disordered proteins. *Proc. Natl. Acad. Sci. U. S. A.* 107(33):14609-14614.
12. Uversky VN (2009) Intrinsically disordered proteins and their environment: effects of strong denaturants, temperature, pH, counter ions, membranes, binding partners, osmolytes, and macromolecular crowding. *Protein J.* 28(7-8):305-325.
13. Zhou HX, Rivas GN, & Minton AP (2008) Macromolecular crowding and confinement: biochemical, biophysical, and potential physiological consequences. *Annu. Rev. Biophys.* 37:375-397.
14. Gershenson A & Gierasch LM (2011) Protein folding in the cell: challenges and progress. *Curr. Opin. Struct. Biol.* 21(1):32-41.
15. Dedmon MM, Patel CN, Young GB, & Pielak GJ (2002) FlgM gains structure in living cells. *Proceedings of the National Academy of Sciences of the United States of America* 99(20):12681-12684.
16. McNulty BC, Young GB, & Pielak GJ (2006) Macromolecular crowding in the Escherichia coli periplasm maintains alpha-synuclein disorder. *Journal of molecular biology* 355(5):893-897.
17. Munishkina LA, Cooper EM, Uversky VN, & Fink AL (2004) The effect of macromolecular crowding on protein aggregation and amyloid fibril formation. *J Mol Recognit* 17(5):456-464.
18. Szasz C*, et al.* (2011) Protein Disorder Prevails under Crowded Conditions. *Biochemistry* 50(26):5834-5844.
19. Hong JA & Gierasch LM (2010) Macromolecular Crowding Remodels the Energy Landscape of a Protein by Favoring a More Compact Unfolded State. *Journal of the American Chemical Society* 132(30):10445-10452.
20. Mikaelsson T, Aden J, Johansson LBA, & Wittung-Stafshede P (2013) Direct Observation of Protein Unfolded State Compaction in the Presence of Macromolecular Crowding. *Biophysical Journal* 104(3):694-704.

21. Johansen D, Jeffries CM, Hammouda B, Trewhella J, & Goldenberg DP (2011) Effects of macromolecular crowding on an intrinsically disordered protein characterized by small-angle neutron scattering with contrast matching. *Biophysical journal* 100(4):1120-1128.
22. Han TNW*, et al.* (2012) Cell-free Formation of RNA Granules: Bound RNAs Identify Features and Components of Cellular Assemblies. *Cell* 149(4):768-779.
23. Li PL*, et al.* (2012) Phase transitions in the assembly of multivalent signalling proteins. *Nature* 483(7389):336-U129.
24. Brangwynne CP (2011) Soft active aggregates: mechanics, dynamics and self-assembly of liquid-like intracellular protein bodies. *Soft Matter* 7(7):3052-3059.
25. Rout MP*, et al.* (2000) The yeast nuclear pore complex: Composition, architecture, and transport mechanism. *J. Cell. Biol.* 148(4):635-651.
26. Elcock AH (2010) Models of macromolecular crowding effects and the need for quantitative comparisons with experiment. *Curr Opin Struc Biol* 20(2):196-206.
27. Hofmann H*, et al.* (2012) Polymer scaling laws of unfolded and intrinsically disordered proteins quantified with single-molecule spectroscopy. *Proc. Natl. Acad. Sci. U. S. A.* 109(40):16155-16160.
28. Soranno A*, et al.* (2012) Quantifying internal friction in unfolded and intrinsically disordered proteins with single molecule spectroscopy. *Proc. Natl. Acad. Sci. U. S. A.* 109(44):17800-17806.
29. Devanand K & Selser JC (1991) Asymptotic-Behavior and Long-Range Interactions in Aqueous-Solutions of Poly(Ethylene Oxide). *Macromolecules* 24(22):5943-5947.
30. Zimmerman SB & Trach SO (1991) Estimation of Macromolecule Concentrations and Excluded Volume Effects for the Cytoplasm of Escherichia-Coli. *Journal of molecular biology* 222(3):599-620.
31. Harris JM (1992) *Poly(Ethylene Glycol) Chemistry: Biotechnical and Biomedical Applications* (Plenum Press, New York).
32. Uversky VN, Gillespie JR, & Fink AL (2000) Why are "natively unfolded" proteins unstructured under physiologic conditions? *Proteins* 41(3):415-427.
33. Mao AH, Crick SL, Vitalis A, Chicoine CL, & Pappu RV (2010) Net charge per residue modulates conformational ensembles of intrinsically disordered proteins. *Proceedings of the National Academy of Sciences of the United States of America* 107(18):8183–8188.
34. Das RK & Pappu RV (2013) Conformations of intrinsically disordered proteins are influenced by linear sequence distributions of oppositely charged residues. *Proc. Natl. Acad. Sci. U S A* 110(33):13392-13397.
35. Ziv G & Haran G (2009) Protein Folding, Protein Collapse, and Tanford's Transfer Model: Lessons from Single-Molecule FRET. *J. Am. Chem. Soc.* 131(8):2942-2947.
36. Cheung MS, Klimov D, & Thirumalai D (2005) Molecular crowding enhances native state stability and refolding rates of globular proteins. *Proceedings of the National Academy of Sciences of the United States of America* 102(13):4753-4758.
37. Minton AP (2005) Models for excluded volume interaction between an unfolded protein and rigid macromolecular cosolutes: Macromolecular crowding and protein stability revisited. *Biophys. J.* 88(2):971-985.
38. Mittal J & Best RB (2010) Dependence of protein folding stability and dynamics on the density and composition of macromolecular crowders. *Biophys. J.* 98(2):315-320.
39. Joanny JF, Grant P, Pincus P, & Turkevich LA (1981) Conformations of Polydisperse Polymer-Solutions - Bimodal Distribution. *J Appl Phys* 52(10):5943-5948.
40. Edwards SF (1966) Theory of Polymer Solutions at Intermediate Concentration. *P Phys Soc Lond* 88(560P):265-&.
41. Schäfer L (1999) *Excluded Volume Effects in Polymer Solutions as Explained by the Renormalization Group* (Springer, Berlin).

42.   Tran HT & Pappu RV (2006) Toward an accurate theoretical framework for describing ensembles for proteins under strongly denaturing conditions. *Biophysical journal* 91(5):1868-1886.

43.   Wilson KG (1983) The Renormalization-Group and Critical Phenomena. *Rev. Mod. Phys.* 55(3):583-600.

44.   Schäfer L & Kappeler C (1993) Interaction Effects on the Size of a Polymer-Chain in Ternary Solutions - a Renormalization-Group Study. *Journal of Chemical Physics* 99(8):6135-6154.

45.   Nose T (1986) Chain Dimension of a Guest Polymer in the Semidilute Solution of Compatible and Incompatible Polymers. *J Phys-Paris* 47(3):517-527.

46.   Minton AP (2013) Quantitative assessment of the relative contributions of steric repulsion and chemical interactions to macromolecular crowding. *Biopolymers* 99(4):239-244.

47.   Sarkar M., Li C., & Pielak GJ (2013) Soft interactions and crowding. *Biophys. Rev.* 5(2):187-194.

48.   Kim YC & Mittal J (2013) Crowding Induced Entropy-Enthalpy Compensation in Protein Association Equilibria. *Phys. Rev. Lett.* 110(20).

49.   Shoemaker BA, Portman JJ, & Wolynes PG (2000) Speeding molecular recognition by using the folding funnel: the fly-casting mechanism. *Proc. Natl. Acad. Sci. U. S. A.* 97(16):8868-8873.

50.   Trizac E, Levy Y, & Wolynes PG (2010) Capillarity theory for the fly-casting mechanism. *Proceedings of the National Academy of Sciences of the United States of America* 107(7):2746-2750.

51.   Schreiber G, Haran G, & Zhou HX (2009) Fundamental Aspects of Protein-Protein Association Kinetics. *Chem Rev* 109(3):839-860.

52.   Vareli K, Frangou-Lazaridis M, van der Kraan I, Tsolas O, & van Driel R (2000) Nuclear distribution of prothymosin alpha and parathymosin: Evidence that prothymosin alpha is associated with RNA synthesis processing and para-thymosin with early DNA replication. *Exp. Cell Res.* 257(1):152-161.

53.   Enkemann SA, Ward RD, & Berger SL (2000) Mobility within the nucleus and neighboring cytosol is a key feature of prothymosin-alpha. *J. Histochem. Cytochem.* 48(10):1341-1355.

54.   Gelman H, Platkov M, & Gruebele M (2012) Rapid perturbation of free-energy landscapes: from in vitro to in vivo. *Chemistry* 18(21):6420-6427.

55.   Phillip Y, Kiss V, & Schreiber G (2012) Protein-binding dynamics imaged in a living cell. *Proc. Natl. Acad. Sci. U. S. A.* 109(5):1461-1466.

56.   Sakon JJ & Weninger KR (2010) Detecting the conformation of individual proteins in live cells. *Nature methods* 7(3):203-205.

57.   Gast K, *et al.* (1995) Prothymosin alpha: a biologically active protein with random coil conformation. *Biochemistry* 34(40):13211-13218.

58.   Zheng R, Jenkins TM, & Craigie R (1996) Zinc folds the N-terminal domain of HIV-1 integrase, promotes multimerization, and enhances catalytic activity. *Proceedings of the National Academy of Sciences of the United States of America* 93(24):13659-13664.

59.   Demarest SJ, *et al.* (2002) Mutual synergistic folding in recruitment of CBP/p300 by p160 nuclear receptor coactivators. *Nature* 415(6871):549-553.

60.   Yi S, Brickenden A, & Choy WY (2008) A new protocol for high-yield purification of recombinant human prothymosin alpha expressed in Escherichia coli for NMR studies. *Protein expression and purification* 57(1):1-8.

61.   Müller BK, Zaychikov E, Bräuchle C, & Lamb DC (2005) Pulsed interleaved excitation. *Biophys. J.* 89(5):3508-3522.

62. Sisamakis E, Valeri A, Kalinin S, Rothwell PJ, & Seidel CAM (2010) Accurate Single-Molecule FRET Studies Using Multiparameter Fluorescence Detection. *Methods Enzymol.* 475:455-514.

63. Strickler SJ & Berg RA (1962) Relationship between Absorption Intensity and Fluorescence Lifetime of Molecules. *Journal of Chemical Physics* 37(4):814-&.

64. Sherman E & Haran G (2006) Coil-globule transition in the denatured state of a small protein. *Proc. Natl. Acad. Sci. U. S. A.* 103(31):11539-11543.

65. Sanchez IC (1979) Phase-Transition Behavior of the Isolated Polymer-Chain. *Macromolecules* 12(5):980-988.

66. Minton AP (1998) Molecular crowding: analysis of effects of high concentrations of inert cosolutes on biochemical equilibria and rates in terms of volume exclusion. *Methods in enzymology* 295:127-149.

67. Boublik T (1974) Statistical Thermodynamics of Convex Molecule Fluids. *Mol. Phys.* 27(5):1415-1427.

68. Oversteegen SM & Roth R (2005) General methods for free-volume theory. *J. Chem. Phys.* 122(21).

69. Qin S & Zhou HX (2013) Effects of Macromolecular Crowding on the Conformational Ensembles of Disordered Proteins. *The journal of physical chemistry letters* 4(20).

70. De Gennes PG (1979) *Scaling concepts in polymer physics* (Cornell University Press, Ithaca, N.Y.).

71. Raphael E, Fredrickson GH, & Pincus P (1992) One Long-Chain among Shorter Chains - the Flory Approach Revisited. *Journal De Physique Ii* 2(10):1811-1823.

72. Kappeler C, Schafer L, & Fukuda T (1991) Light-Scattering from Ternary Polymer-Solutions - an Analysis of the Apparent Radius of Gyration. *Macromolecules* 24(10):2715-2718.

73. Ferry Kienberger*, et al.* (2000) Static and Dynamical Properties of Single Poly(Ethylene Glycol) Molecules Investigated by Force Spectroscopy. *Single Molecules* 1(2):123-128.

74. Kuga S (1981) Pore-Size Distribution Analysis of Gel Substances by Size Exclusion Chromatography. *J. Chromatogr.* 206(3):449-461.

75. Hosek M & Tang JX (2004) Polymer-induced bundling of F actin and the depletion force. *Phys. Rev. E* 69(5).

76. Hammouda B (1993) Sans from Homogeneous Polymer Mixtures - a Unified Overview. *Adv. Polym. Sci.* 106:87-133.

77. Sickmeier M*, et al.* (2007) DisProt: the database of disordered proteins. *Nucleic Acids Res.* 35:D786-D793.

78. Kyte J & Doolittle RF (1982) A simple method for displaying the hydropathic character of a protein. *J. Mol. Biol.* 157(1):105-132.

79. Milles S & Lemke EA (2011) Single molecule study of the intrinsically disordered FG-repeat nucleoporin 153. *Biophys. J.* 101(7):1710-1719.

80. Rout MP, Aitchison JD, Magnasco MO, & Chait BT (2003) Virtual gating and nuclear transport: the hole picture. *Trends Cell Biol.* 13(12):622-628.

81. Alber F*, et al.* (2007) The molecular architecture of the nuclear pore complex. *Nature* 450(7170):695-701.

82. Kato M*, et al.* (2012) Cell-free Formation of RNA Granules: Low Complexity Sequence Domains Form Dynamic Fibers within Hydrogels. *Cell* 149(4):753-767.

83. Kato Y & Nakamura A (2012) Roles of cytoplasmic RNP granules in intracellular RNA localization and translational control in the Drosophila oocyte. *Dev. Growth Differ.* 54(1):19-31.